

## Article

# Numerical Analysis of Instability Mechanism of a High Slope under Excavation Unloading and Rainfall

Manli Qu \* and Faning Dang

School of Civil Engineering and Architecture, Xi'an University of Technology, Xi'an 710048, China

\* Correspondence: 1160412044@stu.xaut.edu.cn

**Abstract:** High slope simulation analysis is an essential means of slope engineering design, construction, and operation management. It is necessary to master slope dynamics, ensure slope safety, analyze slope instability mechanisms, and carry out slope stability early warning and prediction. This paper, aiming at the landslide phenomenon of the high slope on the left bank of a reservoir project, considering the influence of stratum lithology, fault, excavation unloading, rainfall, and water storage, establishes a refined finite element model that reflects the internal structure of the slope. The fluid-solid coupling numerical simulation analysis of the high slope is carried out. Based on this, the failure mechanism of the slope under excavation unloading and heavy rainfall is explained. The application of an engineering example shows that under the combined action of excavation unloading and rainfall infiltration, the in-plane saturation of the structure formed at fault at the trailing edge of the excavation slope surface increases, the pore water pressure increases, and the shear strain concentration area appears at the internal structural surface of the slope. The shear strain concentration area extends along the structural surface to the front and rear edges of the slope, resulting in landslide damage.

**Keywords:** landslide; excavation; rainfall; hydraulic engineering; high slope



**Citation:** Qu, M.; Dang, F. Numerical Analysis of Instability Mechanism of a High Slope under Excavation Unloading and Rainfall. *Appl. Sci.* **2022**, *12*, 7990. <https://doi.org/10.3390/app12167990>

Academic Editors: Yougang Sun, Xinwei Yao and Xiaogang Jin

Received: 12 July 2022

Accepted: 3 August 2022

Published: 10 August 2022

**Publisher's Note:** MDPI stays neutral with regard to jurisdictional claims in published maps and institutional affiliations.



**Copyright:** © 2022 by the authors. Licensee MDPI, Basel, Switzerland. This article is an open access article distributed under the terms and conditions of the Creative Commons Attribution (CC BY) license (<https://creativecommons.org/licenses/by/4.0/>).

## 1. Introduction

According to the environmental objectives of the 2030 agenda for sustainable development, building infrastructure with disaster resilience, promoting inclusive and sustainable industrialization, and promoting innovation are the main objectives [1]. Slope stability is one of the main means of ensuring the ability of infrastructure to resist disasters. Landslides are the fourth most fatal natural disaster after floods, storms, and earthquakes. It has comprehensive coverage, high frequency, and incredible destructive power and can seriously endanger human life and property [1–3]. The evolution of landslides is closely related to geological structure conditions [2,3], seismic activities [4,5], rainfall [6], human activities [7], and other factors. The rock slope is an essential structure in hydropower engineering [8]. It plays a role in bearing the thrust of the dam and preventing water seepage [8,9]. Due to complex geological processes, many joints are often developed in the rock slope, which threatens the slope's stability during construction and operation [6]. Under complex geological conditions in mountainous areas, the stability of the slope is affected by many factors. Based on the analysis and numerical analysis of the actual rock mass structure of the slope, the instability mechanism of the slope under the influence of the double factors of excavation and rainwater infiltration is studied, which has reference significance in the analysis of slope stability [10].

In slope engineering, the rock mass stress near the excavation face is redistributed due to the disturbance of excavation to the rock mass. Its mechanical characteristics are significant areas of unloading [11]. Unloading causes the rapid deterioration of rock mass quality [12]. Therefore, unloading should be considered in the stability analysis of unloaded rock slope [13]. Rock mass excavation must undergo the dynamic change process

of unloading, deformation damage, and deterioration of rock mass mechanical conditions. Its dynamic stability in the excavation process is a problem worthy of study. After slope excavation, the rock mass is unloaded and damaged, the joint connectivity increases, and the rock mass quality deteriorates [8]. The unloading degree of rock mass in different areas is different, and with the progress of excavation, the unloading area and unloading degree of rock mass are constantly changing [9]. Therefore, the simulation process of unloading analysis should be a dynamic process of continuous adjustment [10]. Li et al. [14] took the three failure modes of the landslide in the Zigui basin of the Three Gorges Reservoir as an example to explain the main factors controlling the reservoir-induced landslide. The research results show that a low water level of 145 m to 155 m dramatically reduces the stability of the bank slope of the Three Gorges reservoir. Chen et al. [15] conducted a series of uniaxial compression tests and conventional creep tests. The results showed that the stress cycle instantaneously increased the strain rate and promoted the sharpening of microcracks, thus improving the efficiency of stress corrosion cracking. Dai et al. [9] conducted a numerical simulation based on the FLAC3D program to study the mechanisms and influencing factors of displacement mutation caused by blasting excavation. The results show that strain energy will accumulate and be stored in the slope rock mass under the compression of in situ stress. When blasting or excavation produces a free surface, the stored rock strain energy under in situ stress is released, resulting in joint opening and displacement mutation of the jointed rock slope. The magnitude of joint opening displacement is positively correlated with the strain energy release rate. Zhu et al. [4] found through the unloading test that the cohesion of the unloading normal stress direct shear test decreased significantly, while the internal friction angle increased slightly, the shear displacement increased linearly at the initial stage of the unloading normal stress, and then rapidly increased nonlinearly before failure. Peng et al. [16] analyzed and compared the deformation characteristics and failure mechanisms of homogeneous loess slopes and double paleosol interlayer loess slopes under different excavation slope angles and believed that the response of lateral horizontal earth pressure in the excavation area was closely related to the failure of the slope.

In addition to the landslide caused by artificial disturbances, such as excavation and blasting, rainfall infiltration is also one of the main factors inducing slope instability [6]. Soil in nature is a loose porous medium [17]. Under rainfall infiltration, the stress and seepage field of the soil slope interact with each other [18], and this interaction between fluid and solid is called fluid–solid coupling. The rainfall-type landslide is mainly affected by stress and seepage fields. The infiltration of rainwater into the soil produces a seepage field. With the continuous infiltration of rainfall, the seepage field changes continuously and then has seepage pressure [19]. Seepage pressure acts on the soil for a long time, which changes the stress field of the ground [20]. The change in the stress field will shift the pore volume of the soil and cause the evolution of the seepage field and the permeability coefficient of the ground. The stress field and seepage field of slope soil are closely related to each other. However, the analysis of slope stability under rainfall infiltration mainly focuses on a single field or indirect coupling analysis. The production of rainfall-type landslides results directly from multi-field coupling [21]. Therefore, it is necessary to study the coupling of the seepage field and stress field of the slope under rainfall conditions. Numerical simulation, especially the fully coupled water force large deformation model, is helpful for correctly simulating the complex failure and post-failure mechanisms of rainfall-induced landslides [22]. By analyzing the measured data, Jia et al. [1] concluded that rainfall has the most significant impact on vertical displacement, accounting for 56.76% of total vertical displacement. However, it is still an elastic displacement, which usually causes minor damage to the slope. Pan et al. [6] conducted mechanical tests on rock samples with different water contents, studied the change law of rock mechanical behavior under the action of water, and established the function of rock water-induced weakening. Zheng et al. [23] found that the stability of rainfall-induced dams is relatively poor based on the collected 1578 dam case studies; with the increase of dam height and storage capacity,

the stability first decreases and then increases; with the increase of dam volume and dam material D50, the stability increases gradually; with the increase of catchment area, the stability decreases gradually. Zhang et al. [24] analyzed slope cracks' development and failure modes and studied the early warning strategy for rainfall-induced fill slope failure. The results show that rainfall-induced loess landslides have hysteresis, and saturation and matrix suction responses are earlier than pore water pressure. The slope is damaged when the saturation and matrix suction are at their maximum and minimum values, respectively. Due to the pore water in the unsaturated soil slopes, the seepage field and stress field cannot be separated in a direct manner. Li et al. [25–27] suggest that the seepage-stress separation method can simulate the slope excavation-rainfall coupling process by analyzing the excavation stress field first and then imposing rainfall on the formed boundary.

The finite element method is a very mature numerical method that has been applied to solve stress distribution and displacement characteristics in rock and soil mass for a long time. It can be used to solve problems of elasticity, elastoplasticity, viscoelastoplasticity, and viscoplasticity [28]. The advantage of the finite element method is that the heterogeneity and discontinuity of the rock and soil mass of the slope are considered in part. The size and distribution of the stress and strain of the rock mass can be given, which avoids the shortcomings of the limit equilibrium analysis method in that the sliding body is regarded as rigid and too simplified. It can make us analyze the deformation and failure mechanism of the slope approximately from the stress and strain, explore the first and most prone to yield failure parts, and identify the parts that need to be strengthened first [29].

In this paper, a fluid-structure coupling numerical simulation analysis is carried out for the landslide phenomenon of a reservoir project's left bank high slope. The influence of formation lithology, fault, excavation unloading, rainfall, and water storage is comprehensively considered to explain the failure mechanism of the slope under the action of excavation unloading and heavy rain. Section 2 introduces the study area and slope deformation. In Section 3, taking a simple two-dimensional slope model as an example, the basic theory of fluid-structure coupling analysis is introduced. In Section 4, the three-dimensional finite element model is introduced. According to the three-dimensional finite element analysis results, the failure mechanism of the slope under the action of excavation and rainfall is explained, and a water storage analysis is carried out. Section 5 presents the research conclusion.

## 2. Project Overview

A water control project is located in the gorge section of the upper reaches of the mainstream of the Hanjiang River and Yangxian, east of the Hanzhong Basin in southern Shaanxi. It focuses on water supply, considers power generation, and improves water transport conditions. It is composed of water retaining structures, water release structures, pump station buildings, navigation structures, and fish passing structures. The dam is a roller-compacted concrete gravity dam with a crest elevation of 455.00 m, a maximum dam height of 63.00 m, and a dam axis length of 349.00 m.

The Hanjiang River flows into the northwest of the dam site area from west to east, and the flow direction turns southeast. The river channel is relatively straight. The riverbed elevation in the dam site area is 402–413 m, and the riverbed width is 160–220 m. The dry water surface of the riverbed is about 405 m. The natural slope of the left bank slope has a strike of approximately  $315^\circ$  and a dip of approximately  $225^\circ$ . The elevation of the top of the riverside slope is 695 m, and the topographic slope is  $37\text{--}39^\circ$ . Large-scale Liushu gully and Daihen gully are developed on both upstream and downstream sides of the slope, with about 750 m and a depth of 10–40 m. There is water all year round. Figure 1 shows the original landform of the left bank slope.



**Figure 1.** Original landform.

The dominant orientation of fissures in the slope area on the left bank is NEE, NNW–NNE, and NWW, with a steep dip angle, and the proportion of the medium steep dip angle accounts for about 90%. The length of the fracture trace in adit is generally less than 5 m, that of surface rock mass is generally less than 10 m, and the fracture surface is mostly flat and rough. The fractures in strongly weathered rock mass are mainly filled with argillaceous and ferromanganese, with a thickness of 3–8 mm. The fissures in the weakly weathered rock mass are mainly filled with ferromanganese and calcareous, with a thickness of 1–5 mm. The cracks in the micro new rock mass are mainly filled with calcareous or no filling, and the width is generally less than 2 mm.

The groundwater in the rock mass of the slope is mainly bedrock fissure water, with a buried depth of 19.2–35.3 m. The underground water level is relatively stable. Under normal conditions, the water level changes by 0.1–0.5 m. After heavy rainfall, the water level changes by 1.0–3.0 m. The strongly weathered rock mass of diorite in the dam site area has medium water permeability. The rock mass in the weakly weathered upper area mainly has weak water permeability, and some parts have medium and slight water permeability. The weakly weathered lower area and micro new rock mass are dominated by micro permeability, followed by weak permeability. The strongly weathered rock mass of diorite on the left bank is 5–34 m thick, the rock mass in the upper weakly weathered area is 5–23 m thick, the rock mass in the lower weakly weathered area is 5.4–34.3 m thick, and the maximum exposed thickness of the lower micro fresh rock mass is 44.5 m. The weathering degree becomes weaker from the slope surface to the inside, and the weathering thickness becomes thicker as elevation increases.

On 10 November 2015, the left bank slope excavation was started. In early April 2016, the left slope was excavated to 506 m. On 14 July 2016, cracks on the left bank slope at 536 m berm and above suddenly widened. During the patrol inspection, the on-site personnel found that there were more cracks on the 553 m berm and the slope above. On 18 July 2016, the construction site began to suffer from a continuous rainstorm. At about 7:40 a.m. on 19 July, the slope body below the elevation of 650 m on the left bank slope collapsed, as shown in Figure 2.



**Figure 2.** Slope collapse.

### 3. Impact of Rainfall on Slope Stability

Rainfall will reduce the shear strength of rock and soil mass, raise the groundwater level [30], and increase pore water pressure. In addition, long-term and high-intensity rainfall will lead to a transient saturation area in the area above the stable groundwater level, and the pore water pressure will rise in the corresponding area [31]. Therefore, it is necessary to study the impact of transient seepage of rainwater infiltration on the stress and strain of soil slope [32]. Here, a typical example is selected for analysis.

#### 3.1. Numerical Simulation Model and Parameters

As shown in Figure 3, the slope toe is  $40^\circ$ , and the slope height is 30 m. The initial groundwater level is level with the slope toe. This example assumes that pore water pressure (including suction) is linearly distributed with depth. See Figure 4 for the variation process of rainfall amplitude simulated for 72 h. The rainfall infiltration intensity of the slope is set at 0.015 m/s, and the rainfall infiltration intensity of the slope top is set at 0.02 m/s. The elastic modulus of the soil used for the calculation is 10 MPa, Poisson's ratio is 0.3, cohesion  $c' = 15$  kPa, and friction angle  $\varphi' = 30^\circ$ .

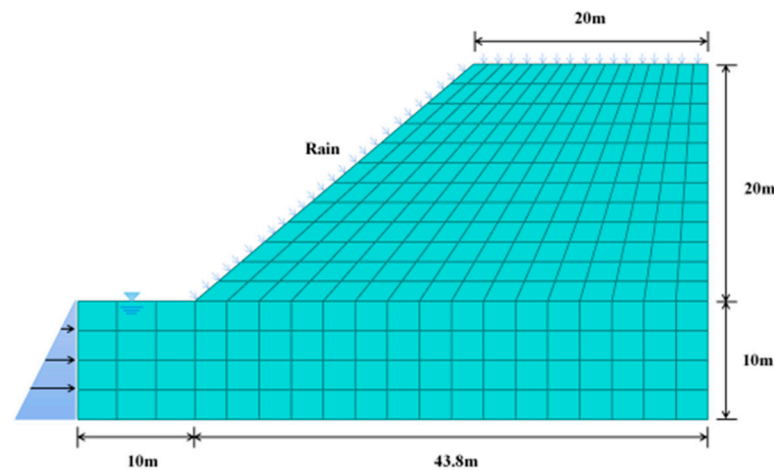


Figure 3. Finite element model.

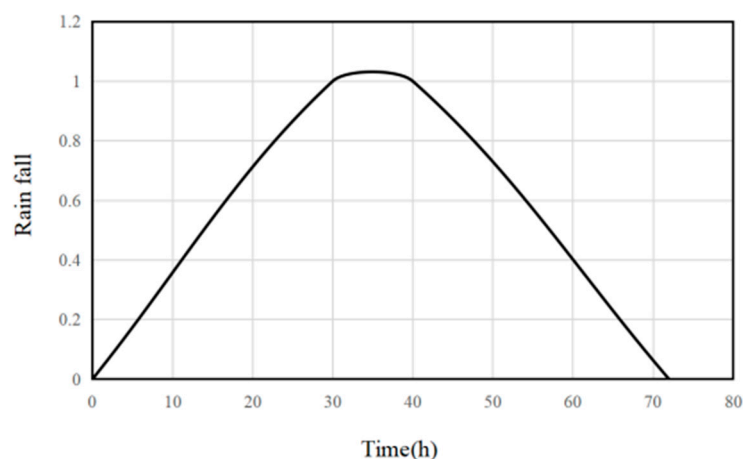


Figure 4. Rainfall intensity amplitude.

The relationship between the material permeability coefficient and the matrix suction is:

$$K_w = a_w K_{ws} / [a_w + (b_w \times (u_a - u_w))^{c_w}] \tag{1}$$

where  $K_{ws}$  is the permeability coefficient when the soil is saturated, taking  $5.0 \times 10^{-6}$  m/s (0.018 m/h).  $u_a$  and  $u_w$  are air pressure and the water pressure in the soil, respectively.

Since the slope surface is in contact with the atmosphere,  $u_a$  is simply taken as 0.  $a_w$ ,  $b_w$ , and  $c_w$  are material coefficients, which are taken as 1000, 0.01, and 1.7, respectively, in this example.

The relationship between saturation and matrix suction is:

$$S_r = S_i + (S_n - S_i)a_s / [a_s + (b_s \times (u_a - u_w))^{c_s}] \tag{2}$$

where  $S_r$  is saturation;  $S_i$  is residual saturation, which is 0.08 in this case;  $S_n$  is the maximum saturation, taken as 1;  $a_s$ ,  $b_s$  and  $c_s$  are material coefficients, which are taken as 1,  $5 \times 10^{-5}$ , 3.5 in this example.

The relationship between the efficiency of capability reduction and matrix suction and water content obtained from the above two formulas is shown in Figure 5.

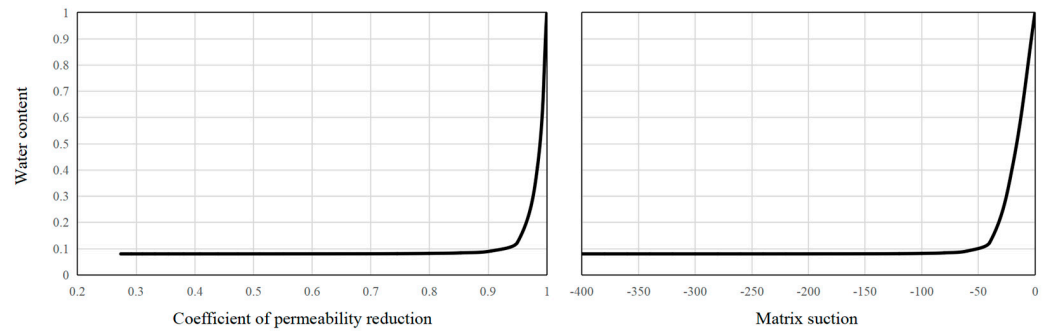


Figure 5. Relationship between coefficient of capability reduction and matrix suction and water content.

### 3.2. Analysis of Calculation Results

Through finite element calculation, the saturation distribution and pore water pressure distribution of the slope before and after rainfall are shown in Figures 6 and 7, and the rainfall flow velocity distribution at the beginning and end of rainfall is shown in Figure 8.

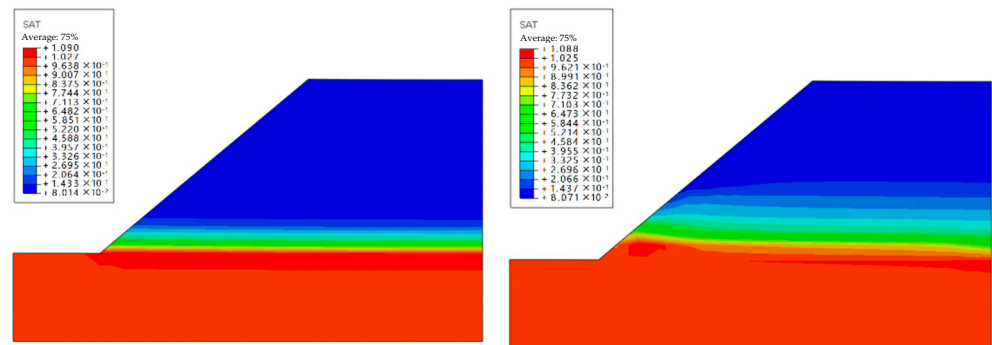


Figure 6. Saturation distribution of slopes before and after rainfall.

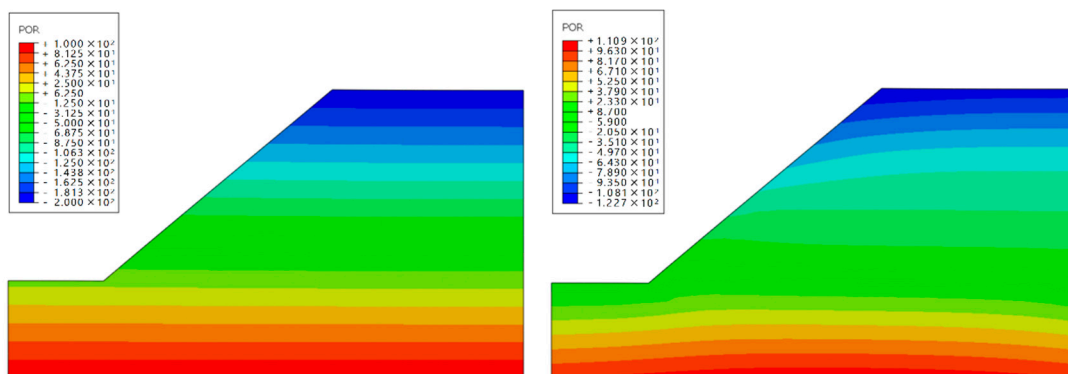
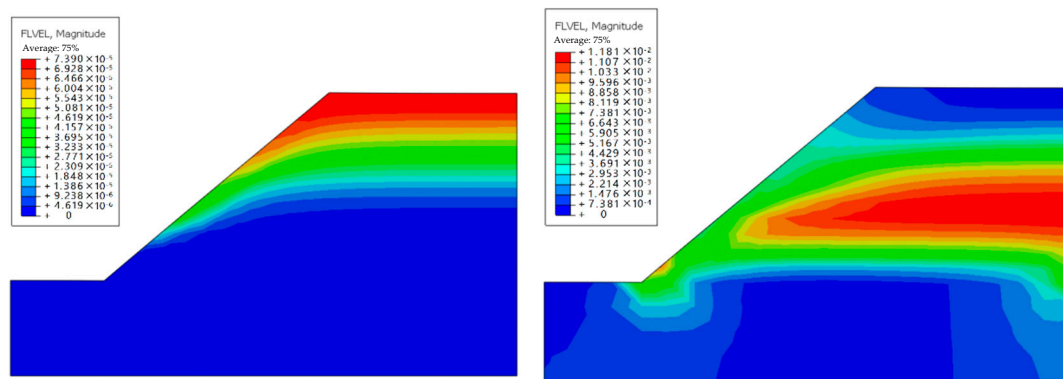


Figure 7. Pore water pressure distribution of the slope before and after rainfall.



**Figure 8.** Internal flow velocity of slope at the beginning and end of rainfall.

According to the above analysis results:

- (1) Considering that the pore water pressure distribution after rainfall infiltration differs from the initial state, the suction area below the top of the slope decreases, and the matrix suction also decreases. Comparing the results at different times, it can be found that with the extension of rainfall time, the saturation increases, the pore water pressure increases, and the matrix suction in shallow soil decreases or disappears. After rainfall decreases or stops, saturation decreases gradually with the extension of time, saturation decreases, pore water pressure drops, and matrix suction in the shallow soil layer increases slowly.
- (2) The maximum horizontal displacement occurs at the slope toe, and the full settlement occurs in the middle of the soil slope. This is because, after rainfall infiltration, suction decreases. The pore pressure increases, the effective stress decreases, and the unloading rebound phenomenon occurs. On the other hand, with rainfall infiltration, soil moisture content and unit weight will increase, leading to heave and stress development. The slope tends to cause sliding deformation due to rainfall infiltration, so it can be considered that slope stability is reduced.
- (3) As the rainfall intensity changes according to the law in Figure 2, it first increases from 0 to the maximum value and then gradually decreases to 0. Therefore, at the beginning of rainfall, rainwater infiltrates downward through the slope and slope top. As the rainfall intensity gradually decreases to 0, the overflow phenomenon occurs at the slope toe, and the flow velocity is largest at the middle elevation inside the slope.
- (4) For the slope toe element, the pore water pressure increases, and the effective average stress decreases under the action of rainfall infiltration. The effective stress path reaches the yield surface when it drops to a certain extent. Currently, the stress path moves to the left and down along the yield surface (Mohr–Coulomb strength envelope) until the rainfall gradually decreases, the suction increases, the pore water pressure drops, and the effective stress increases gradually shifts to the yield surface. For the internal unit of the soil slope, the unit weight above the unit increases after water absorption, increasing the average effective stress and partial stress. Until the later stage of rainfall, adequate moderate pressure and partial stress decrease near the end of the rains. This also confirms the view of some scholars that instability may occur mainly in the shallow layer of the slope under the action of rainfall infiltration [18,19].

## 4. Numerical Simulation Analysis of Slope Instability

### 4.1. Finite Element Model

The overall three-dimensional numerical model of the slope is established according to the geological engineering conditions exposed during the excavation and slope cleaning of the left bank slope, as well as the original terrain and construction excavation form before the damage, as shown in Figure 9a. The slope excavation process is simulated in the

calculation according to the original design scheme. The simulated excavation is from 590 m to 470 m platform. See Figure 9b for the model after excavation.

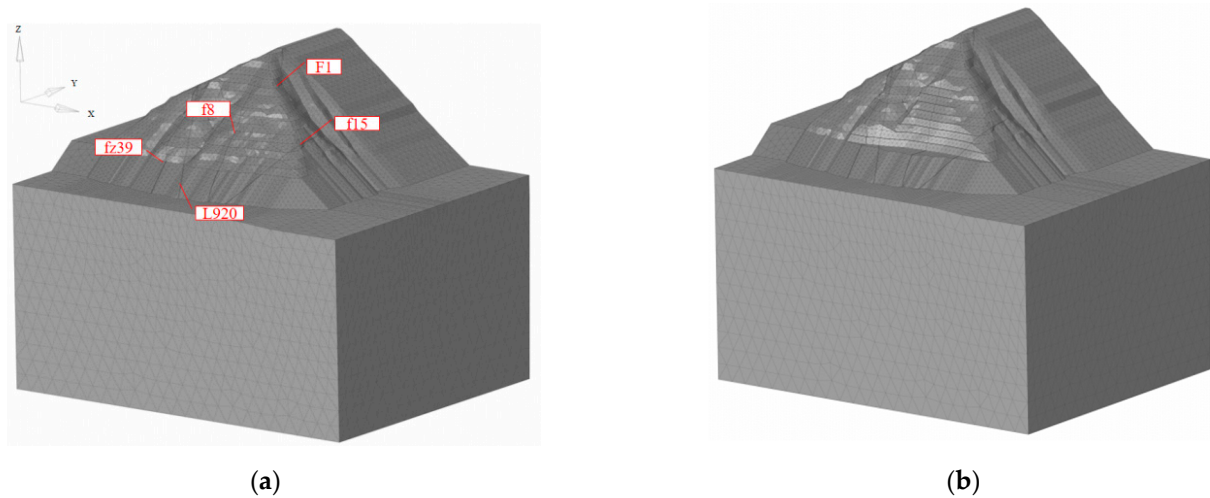


**Figure 9.** Three-dimensional numerical model of the left bank slope. (a) before excavation. (b) after excavation.

In the model, the *x*-axis is along the river and points downstream as positive; the *Y* axis is the dam axis direction; the direction pointing to the inner side of the mountain is positive; the *Z* axis is the numerical direction; and the vertical direction is positive. The calculation range of the *Y* axis is 916 m and 728 m, respectively, and the calculation range of the *Z* axis is from an elevation of  $-106$  m to the surface. The maximum elevation difference of the slope body is 801 m. The model has 174,097 units and 31,662 nodes. The rock stratum involved in the model is mainly diorite, divided into four layers from top to bottom: strongly weathered area, weakly weathered upper area, weakly weathered lower area, and micro new rock mass. Adverse structural planes, such as F1, F15, F8, fz39, and L920, are mainly considered.

4.2. Slope Material Properties

The ideal elastoplastic model with the Mohr–Coulomb criterion as the yield function is adopted for each rock mass. Mohr–Coulomb failure criterion is a set of linear equations without considering the intermediate principal stress of rock materials, which can be used to judge whether rock materials are damaged. See Table 1 for the specific material parameters used in the numerical simulation.

**Table 1.** Strength parameters of slope materials.

Rock Mass and Fault Zoning	Severe	Deformation Parameters		Strength Parameters	
	$\gamma/(\text{kN/m}^3)$	<i>E</i> /GPa	Poisson's Ratio $\mu$	$f' / ^\circ$	$c' / \text{MPa}$
Intensely weathered	26.5	0.5	0.32	24	0.15
Weakly weathered upper layer	28.2	4.5	0.27	40	0.8
Weakly weathered lower layer	28.4	6.5	0.26	45	0.9
Micro new rock	28.5	18.0	0.25	50	1.1
f8	27.0	0.5	0.32	15	0.24
F1	26.0	0.5	0.32	16	0.25
f15	26.0	0.5	0.28	16	0.3
f39-1/f39	26.0	0.5	0.32	16	0.22
L920	27.0	3.5	0.26	23	0.75

4.3. Calculation Conditions and Boundary Conditions

The life and death element functions are used to simulate bank slope excavation. During the simulation process, the excavated slope soil element is deleted layer by layer

according to the actual construction sequence to analyze the impact of bank slope excavation on its disturbance.

In the reservoir impounding analysis, the influence of impounding on the left bank slope is analyzed from no water to 450 m (normal pool level).

The initial in situ stress is only considered a self-weight stress field without considering tectonic action. The slope surface is free, the foundation bottom is fixed and restrained, and normal constraints surround the foundation. During rainfall and water storage analysis, the initial groundwater level is set to a level with the slope toe, and the pore water pressure (including suction) is linearly distributed with depth. As the slope angle changes little, the rainfall infiltration intensity on the slope is uniformly set at 0.02 m/s.

#### 4.4. Analysis of Finite Element Simulation Results

##### 4.4.1. Initial Ground Stress

Through the initial ground stress analysis, the initial ground stress field of the high slope on the left bank is formed, as shown in Figure 10. The displacement distribution characteristics before and after balance under the action of self-weight are shown in Figure 11.

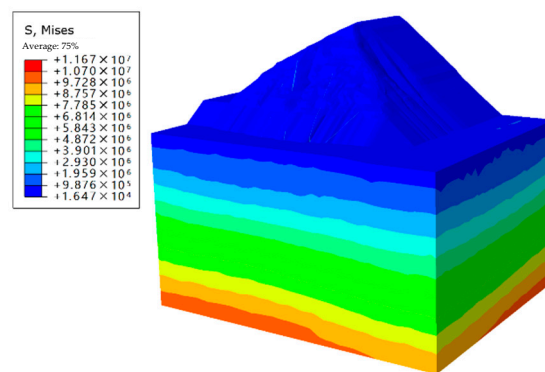


Figure 10. Initial ground stress distribution.

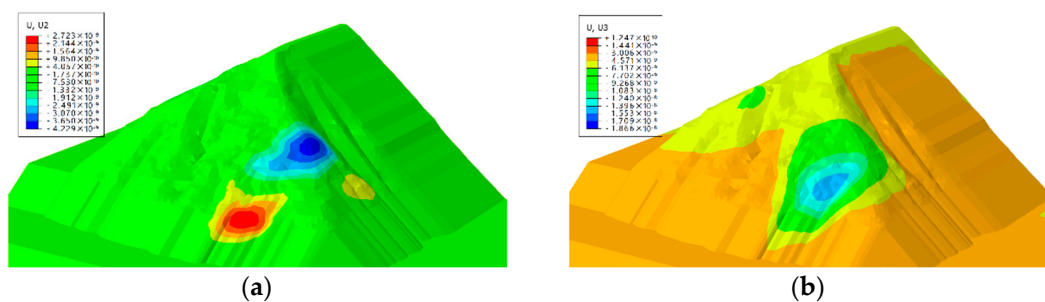
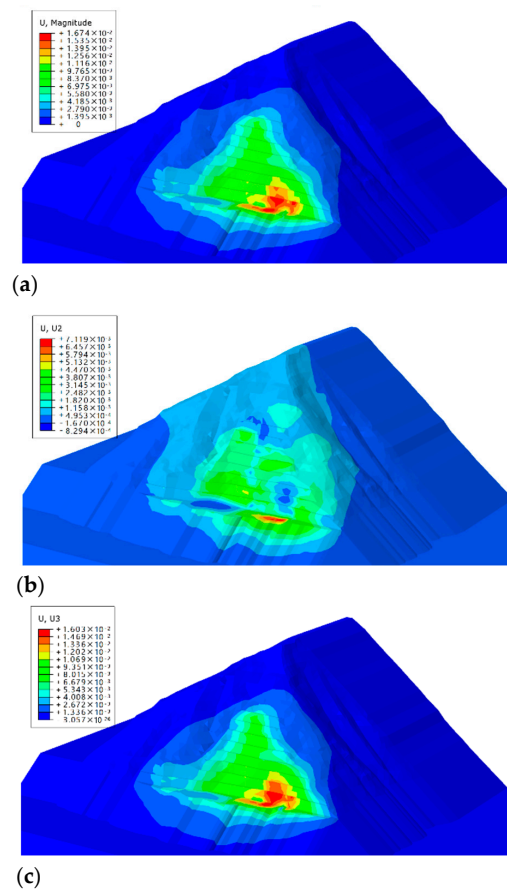


Figure 11. Distribution characteristics of initial displacement. (a) Displacement along slope. (b) vertical displacement.

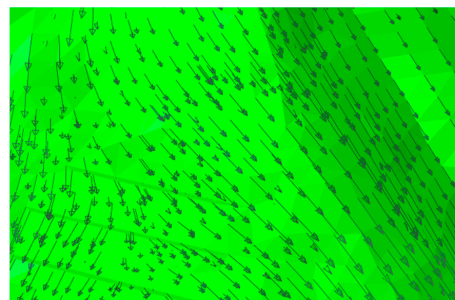
It can be seen from Figures 10 and 11 that under the action of self-weight, the initial ground stress of the left bank slope is larger below the slope, and smaller at the river valley and the deeper Daihen ditch, which conforms to the characteristics of ground stress distribution. The river valley and initial displacement are mainly vertical, and the area with relatively large displacement is concentrated primarily on the higher ridge on the upstream side and the block surrounded by faults FZ8 and F15.

##### 4.4.2. Slope Instability Analysis

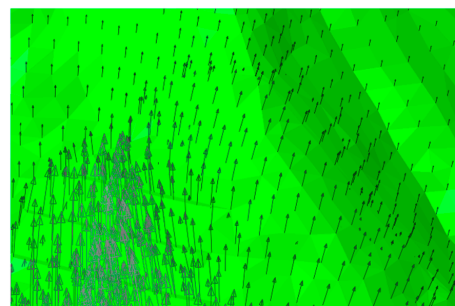
Figure 12 shows the displacement distribution characteristics after excavation, and Figure 13 shows the surface displacement vector diagram.



**Figure 12.** Displacement distribution after excavation. (a) Resultant displacement. (b) Displacement along slope direction. (c) Vertical displacement.



(a)



(b)

**Figure 13.** Displacement vector diagram after excavation. (a) Slope surface displacement at the beginning of excavation. (b) Slope surface displacement after balance after excavation.

According to the finite element calculation results:

- (1) After the completion of the excavation, due to the influence of excavation unloading, the settlement and deformation of the left bank slope recover rapidly. Relative to the initial in situ stress state, the displacement is mainly vertical and upward, indicating that under excavation unloading, the left bank slope has rebounded in the excavation range and nearby soil. Due to the poor mechanical properties of the rock mass in the upper strongly weathered area, the slope in the strongly weathered area is mainly deformed along the slope direction, and the excavated slope in other parts is mainly deformed by unloading and rebounding toward the excavation free face. At the initial stage of excavation, the surface deformation of the slope mainly occurs downward, and the displacement of the slope before excavation is significantly greater than that after excavation. In the later stage of excavation, the whole body moves upward, and the displacement within the excavation range is significantly greater than that of the other parts.
- (2) When the excavation is completed, and the whole slope is balanced, the incremental deformation of the slope is between 3–160 mm, and the maximum value mainly occurs in the block with an elevation of 465–480 m and is surrounded by faults FZ8 and F15. The deformation of the front edge of the excavated slope is significant, and the rear rim is small.
- (3) It is worth noting that in the displacement along the slope, there is a prominent area with large displacement at an elevation of about 615 m above the upper edge of the excavation. The displacement along the slope is about 1.5–2.5 times that of the excavation platform at an elevation of 590 m. This phenomenon may be caused by rebound deformation of the foundation soil due to excavation unloading. However, due to the existence of fault F1, the deformation is not coordinated, and the fault interior becomes loose. This may be one of the geological causes of the landslide on 19 July 2016.

The slope stability is analyzed through the shear strain concentration area caused by rainfall after excavation. Figure 14 shows the slope plastic area distribution characteristics after recess, and Figure 15 shows the shear strain rate concentration area development after rain.

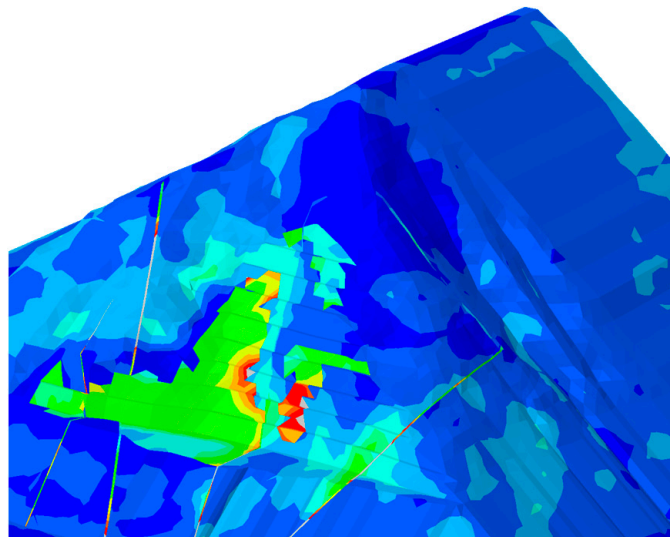


**Figure 14.** Distribution of slope plastic area.

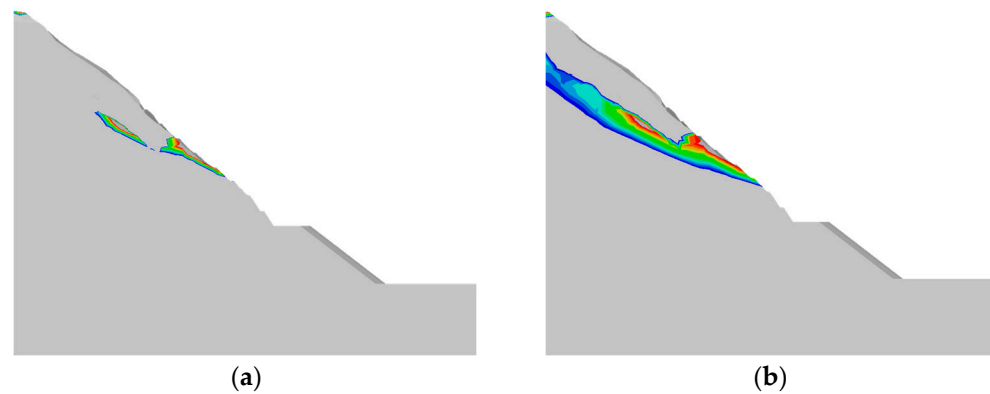


**Figure 15.** Development process of shear strain rate concentration area. (a) Distribution of plastic zone in slope during early rainfall. (b) Distribution of plastic zone in slope at the end of rainfall.

The results show that with rainfall infiltration, the shear strain concentration area first appears at the internal structural plane of the slope and extends along the structural plane to the front and back edges of the slope. When the excavation is completed and balanced, the shear strain concentration area penetrates the entire excavation slope. The plastic area of the slope is dominated by shear yield. Tension shear yield exists locally at the structural plane and the excavation-free face. After the excavation is completed and balanced, the rock mass above the fault has entered the plastic yield state, and the slope is close to the critical state at this stage.

#### 4.4.3. Safety Factor of Slope Stability

The essence of the sliding failure of the slope is strength failure caused by insufficient shear strength of rock and soil mass or structural plane [8]. Therefore, the strength reduction method is used to recheck the safety factor of slope stability. In the numerical calculation, the non-convergence of the analysis, the inflection points of the relation curve between the displacement of the key points of the slope and the strength reduction coefficient, and the penetration of the shear strain concentration area are used to judge whether the slope has entered the critical state comprehensively.

The strength reduction method is used to calculate the safety factor of slope stability. The shear strength reduction factor is defined as the ratio of the maximum shear strength provided by the soil in the slope to the actual shear stress generated by the external load when the external load remains unchanged. The strength reduction method is used to calculate the safety factor of slope stability by continuously reducing the  $c$  and  $\varphi$  value of materials. The reduced shear strength parameters can be expressed as:

$$c_m = c/F_r \quad (3)$$

$$\varphi_m = \arctan(\tan \varphi/F_r) \quad (4)$$

where  $c_m$  and  $\varphi_m$  are the shear strength required to maintain equilibrium or exerted by the soil mass.  $F_r$  is the strength reduction factor.

The original model, the first excavation model, and the second excavation model are used to calculate the stability safety factor of the slope. In the calculation of each model,  $F_r$  is set to increase linearly from 0.75 to 2.5 until it does not converge and the safety factor is calculated, and the safety factors of slope stability under different working conditions are shown in Table 2.

**Table 2.** Strength parameters of slope materials.

Model Type	Calculated Safety Factor	Tolerable Safety Factor	
Original model	1.09	0.5	1.35
First Excavation Model	1.10	4.5	1.35
Second Excavation Model	1.27	3.5	1.35

According to the analysis results in Table 2, the calculation results show that the safety factor before slope excavation is 1.09; After the bank slope is cut for the first time and the load is reduced, the safety factor is only increased to 1.10. Since bolt support is not considered in the calculation, the safety factor of the slope is low. Compared with the tolerable safety factor, the calculated safety factor of all models is small to meet the safety requirements of slope stability.

To sum up, for typical structural plane-controlled slopes, excavation unloading deformation is mainly represented by structural plane deformation. The slope deformation is composed chiefly of structural plane dislocation deformation. Structural plane deformation is primarily controlled by the exposure of the structural plane when excavating the free face, excavation unloading scale, etc. Therefore, it is reasonable to adopt “load reduction” measures in combination with the block shape of “wide at the top and narrow at the bottom, top heavy and foot light”.

## 5. Conclusions

In this paper, a fluid-structure coupling numerical simulation analysis is carried out for the landslide phenomenon of a reservoir project’s left bank high slope. The influence of formation lithology, fault, excavation unloading, rainfall, and water storage is comprehensively considered to explain the failure mechanism of the slope under the action of excavation unloading and heavy rain. The main conclusions are as follows:

- (1) With the extension of rainfall time, saturation increases, pore water pressure increases, and matrix suction in shallow soil decreases or disappears. After rainfall decreases or stops, saturation decreases gradually with the extension of time, pore water pressure drops, and matrix suction in the shallow soil layer increases slowly.
- (2) Under the action of excavation unloading, the high slope rebounds and deforms, resulting in a loose structural plane at fault F1 at the back edge of the excavated slope. Under the action of rainfall infiltration, saturation in the structural plane increases, and pore water pressure increases. With rainfall infiltration, the shear strain concentration area first appears at the inner structural plane of the slope. It extends along the structural plane to the front and rear edges of the slope, resulting in landslide failure of the slope.
- (3) For the typical structural plane-controlled slope, excavation unloading deformation is mainly represented by structural plane deformation. The slope deformation is composed chiefly of the structural plane dislocation deformation. Structural plane deformation is primarily controlled by the exposure of the structural plane when excavating the free face, excavation unloading scale, etc. The shear failure and unstable displacement caused by excavation unloading are the leading causes of landslides.
- (4) The unloading deformation of slope excavation is mainly manifested as the deformation of the structural plane, and the slope deformation is composed chiefly of the dislocation deformation of the structural plane. The deformation of the structural plane is mainly controlled by the exposure of the structural plane in excavating the free surface and the scale of excavation unloading. In practical applications, load-reduction measures can be used to improve the stability of the slope.

**Author Contributions:** Conceptualization, M.Q. and F.D.; methodology, M.Q.; software, M.Q.; validation, M.Q. and F.D.; formal analysis, M.Q.; investigation, M.Q.; resources, M.Q.; data curation, M.Q.; writing—original draft preparation, M.Q.; writing—review and editing, M.Q.; visualization, M.Q.; supervision, F.D.; project administration, F.D.; funding acquisition, F.D. All authors have read and agreed to the published version of the manuscript.

**Funding:** This research was supported by the National Natural Science Foundation of China (No. 51979225).

**Data Availability Statement:** The dataset used to support the findings of this study is available from the corresponding author upon request.

**Conflicts of Interest:** The authors declare that there is no conflict of interest.

## References

- Lee, B.X.; Kjaerulf, F.; Turner, S.; Cohen, L.; Donnelly, P.D.; Muggah, R.; Davis, R.; Realini, A.; Kieselbach, B.; MacGregor, L.S. Transforming our world: Implementing the 2030 agenda through sustainable development goal indicators. *J. Public Health Policy* **2016**, *37*, 13–31. [[CrossRef](#)]
- Torres-Suarez, M.C.; Alarcon-Guzman, A.; Moya, B.D. Effects of loading-unloading and wetting-drying cycles on geomechanical behaviors of mudrocks in the Colombian Andes. *J. Rock Mech. Geotech. Eng.* **2014**, *6*, 257–268. [[CrossRef](#)]
- Zhang, J.; Kuang, M.; Zhang, Y.; Feng, T. Evaluation and analysis of the causes of a landslide and treatment measures during the excavation of a tunnel through a soil-rock interface. *Eng. Fail. Anal.* **2021**, *130*, 105784. [[CrossRef](#)]
- Zhu, T.; Huang, D. Experimental investigation of the shear mechanical behavior of sandstone under unloading normal stress. *Int. J. Rock Mech. Min. Sci.* **2019**, *114*, 186–194. [[CrossRef](#)]
- Xu, J.; Ueda, K.; Uzuoka, R. Numerical modeling of seepage and deformation of unsaturated slope subjected to post-earthquake rainfall. *Comput. Geotech.* **2022**, *148*, 104791. [[CrossRef](#)]
- Pan, Y.; Wu, G.; Zhao, Z.; He, L. Analysis of rock slope stability under rainfall conditions considering the water-induced weakening of rock. *Comput. Geotech.* **2020**, *128*, 103806. [[CrossRef](#)]
- Zhang, F.; Liu, G.; Chen, W.; Liang, S.; Chen, R.; Han, W. Human-induced landslide on a high cut slope: A case of repeated failures due to multi-excavation. *J. Rock Mech. Geotech. Eng.* **2012**, *4*, 367–374. [[CrossRef](#)]
- Wang, S.; Xu, W.; Yan, L.; Feng, X.-T.; Xie, W.-C.; Chen, H. Experimental investigation and failure mechanism analysis for dacite under true triaxial unloading conditions. *Eng. Geol.* **2019**, *264*, 105407. [[CrossRef](#)]
- Dai, J.; Yang, J.; Yao, C.; Hu, Y.; Zhang, X.; Jiang, Q.; Zhou, C. Study on the mechanism of displacement mutation for jointed rock slopes during blasting excavation. *Int. J. Rock Mech. Min. Sci.* **2022**, *150*, 105032. [[CrossRef](#)]
- Li, C.; Fu, Z.; Wang, Y.; Tang, H.; Yan, J.; Gong, W.; Yao, W.; Criss, R.E. Susceptibility of reservoir-induced landslides and strategies for increasing the slope stability in the Three Gorges Reservoir Area: Zigui Basin as an example. *Eng. Geol.* **2019**, *261*, 105279. [[CrossRef](#)]
- Wyllie, D.C.; Mah, C. *Rock Slope Engineering*; CRC Press: Boca Raton, FL, USA, 2004.
- Shen, J.H.; Wang, L.S.; Wang, Q.H.; Xu, J.; Jiang, Y.S.; Sun, B.J. Deformation and fracture features of unloading rock mass. *Chin. J. Rock Mech. Eng.* **2003**, *22*, 2028–2031.
- Ha, Q.L. Simulation analysis of rock mass engineering and rock mass mechanic. *Chin. J. Geotech. Eng.* **2001**, *23*, 664–668.
- Li, J.L.; Ha, Q.L. The three dimensions numerical model of unloading rock mass mechanics parameters related to three-gorges. *J. Univ. Hydr. Elec. Eng.* **1997**, *19*, 1–6.
- Chen, C.; Xu, T.; Heap, M.J.; Baud, P. Influence of unloading and loading stress cycles on the creep behavior of Darley Dale Sandstone. *Int. J. Rock Mech. Min. Sci.* **2018**, *112*, 55–63. [[CrossRef](#)]
- Peng, J.; Fan, Z.; Wu, D.; Huang, Q.; Wang, Q.; Zhuang, J.; Che, W. Landslides triggered by excavation in the loess plateau of China: A case study of Middle Pleistocene loess slopes. *J. Asian Earth Sci.* **2019**, *171*, 246–258. [[CrossRef](#)]
- Zhang, Y.; Jiang, H.; Bai, G.; Han, B. Coupling Action of rainfall and vehicle loads impact on the stability of loess slopes based on the iso-water content layer. *Earthq. Res. Adv.* **2022**, *2*, 100143. [[CrossRef](#)]
- Li, Q.; Song, D.; Yuan, C.; Nie, W. An image recognition method for the deformation area of open-pit rock slopes under variable rainfall. *Measurement* **2022**, *188*, 110544. [[CrossRef](#)]
- Gao, Q.F.; Zeng, L.; Shi, Z.N. Effects of desiccation cracks and vegetation on the shallow stability of a red clay cut slope under rainfall infiltration. *Comput. Geotech.* **2021**, *140*, 104436. [[CrossRef](#)]
- Chang, Z.; Huang, F.; Huang, J.; Jiang, S.-H.; Zhou, C.; Zhu, L. Experimental study of the failure mode and mechanism of loess fill slopes induced by rainfall. *Eng. Geol.* **2021**, *280*, 105941. [[CrossRef](#)]
- Song, X.; Tan, Y. Experimental study on failure of temporary earthen slope triggered by intense rainfall. *Eng. Fail. Anal.* **2020**, *116*, 104718. [[CrossRef](#)]
- Cuomo, S.; Di Perna, A.; Martinelli, M. Modelling the spatio-temporal evolution of a rainfall-induced retrogressive landslide in an unsaturated slope. *Eng. Geol.* **2021**, *294*, 106371. [[CrossRef](#)]

23. Zheng, H.; Shi, Z.; Shen, D.; Peng, M.; Hanley, K.J.; Ma, C.; Zhang, L. Recent advances in stability and failure mechanisms of landslide dams. *Front. Earth Sci.* **2021**, *9*, 659935. [[CrossRef](#)]
24. Zhang, S.; Zhang, X.; Pei, X.; Wang, S.; Huang, R.; Xu, Q.; Wang, Z. Model test study on the hydrological mechanisms and early warning thresholds for loess fill slope failure induced by rainfall. *Eng. Geol.* **2019**, *258*, 105135. [[CrossRef](#)]
25. Li, Q.; Wang, Y.M.; Zhang, K.B.; Yu, H.; Tao, Z.Y. Field investigation and numerical study of a siltstone slope instability induced by excavation and rainfall. *Landslides* **2020**, *17*, 1485–1499. [[CrossRef](#)]
26. Yu, X.; Gong, B.; Tang, C. Study of the slope deformation characteristics and landslide mechanisms under alternating excavation and rainfall disturbance. *Bull. Eng. Geol. Environ.* **2021**, *80*, 7171–7191. [[CrossRef](#)]
27. Xu, X.; Xing, Y.; Guo, Z.; Huang, Y. Stability analysis of rainfall-triggered toe-cut slopes and effectiveness evaluation of pile-anchor structures. *J. Earth Sci.* **2021**, *32*, 1104–1112. [[CrossRef](#)]
28. Yadav, O.P.; Jiwari, R. A finite element approach for analysis and computational modelling of coupled reaction diffusion models. *Numer. Methods Partial. Differ. Equ.* **2019**, *35*, 830–850. [[CrossRef](#)]
29. Yadav, O.P.; Jiwari, R. A finite element approach to capture Turing patterns of autocatalytic Brusselator model. *J. Math. Chem.* **2019**, *57*, 769–789. [[CrossRef](#)]
30. Greco, R.; Comegna, L.; Damiano, E.; Marino, P.; Olivares, L.; Santonastaso, G.F. Recurrent rainfall-induced landslides on the slopes with pyroclastic cover of Partenio Mountains (Campania, Italy): Comparison of 1999 and 2019 events. *Eng. Geol.* **2021**, *288*, 106160. [[CrossRef](#)]
31. Fang, Q.; Zhao, L.; Hou, R.; Fan, C.; Zhang, J. Rainwater transformation to runoff and soil loss at the surface and belowground on soil-mantled karst slopes under rainfall simulation experiments. *CATENA* **2022**, *215*, 106316. [[CrossRef](#)]
32. Tang, G.; Huang, J.; Sheng, D.; Sloan, S.W. Stability analysis of unsaturated soil slopes under random rainfall patterns. *Eng. Geol.* **2018**, *245*, 322–332. [[CrossRef](#)]